

Channel Eigenvalues and Effective Degrees of Freedom of Reconfigurable Intelligent Surfaces

Shu Sun, *Member, IEEE*

Abstract

As a promising candidate technology for the next-generation wireless communications, reconfigurable intelligent surface (RIS) has gained tremendous research interest in both the academia and industry in recent years. Only limited knowledge, however, has been obtained about the channel eigenvalue characteristics and degrees of freedom (DoF) of systems containing RISs. In this paper, we focus on a wireless communication system where both the transmitter and receiver are respectively equipped with an RIS. Features of eigenvalues, such as their summation and individual behavior, are investigated for both the correlation matrix of an RIS and the composite channel matrix encompassing the two RISs and the wireless channel. Furthermore, the concept of effective degrees of freedom (EDoF), i.e., the number of subchannels actively contributing to conveying information, is revisited for RIS-enabled systems. Analytical and numerical results demonstrate that the EDoF depends upon various factors including the operating SNR, physical parameters of RISs, and propagation environment.

Index Terms

Channel model, eigenvalue, reconfigurable intelligent surface (RIS), small-scale fading, degrees of freedom.

I. INTRODUCTION

Massive MIMO (multiple-input multiple-output) [1] is a pivotal physical-layer technology for the fifth-generation (5G) and beyond-5G wireless systems, which can bring immense advantages in spectral efficiency and energy efficiency [1]–[5]. In typical Massive MIMO antenna arrays, the adjacent element spacing is usually half-wavelength or larger. As a natural extension of Massive MIMO, more elements may be arranged in a small form factor if the element spacing further

Shu Sun is with the Department of Electronic Engineering, Shanghai Jiao Tong University, Shanghai, China (e-mail: ss7152@nyu.edu).

decreases from the half-wavelength, where the whole array can be looked upon as a spatially-continuous electromagnetic aperture in its eventual form [6]. This type of extended Massive MIMO is named Holographic MIMO [6], [7]. On the other hand, reminiscent to metasurfaces in the optical field [8], [9], the sub-wavelength pattern has the potential to control incoming electromagnetic waves via anomalous reflection, refraction, polarization transformation, and other functionalities, for wireless communication purposes. Consequently, such kind of architecture is also referred to as large intelligent surface, intelligent metasurface, reconfigurable intelligent surface (RIS), among other names. In this paper, we utilize RIS as the umbrella term for all the two-dimensional (2D) sub-wavelength structures mentioned above. In order to unleash the full potentials of the RIS technology, it is necessary to understand its fundamental properties, such as the associated channel eigenvalues and spatial degrees of freedom (DoF).

Despite the proliferation in research interests of RIS, only limited works are available in the open literature on characterizing the eigenvalue features and DoF of RIS channels. Due to the small (generally no larger than a half-wavelength) element spacing in an RIS, the spatial correlation is non-zero even under isotropic scattering [6], [10], [11]. Among the early works involving antenna spatial correlation, the authors of [12] have considered spatial correlation among multielement antennas, and derived upper and lower capacity bounds taken into account antenna correlation. Fading correlation has also been explored in [13] to examine the capacity growth with respect to the number of antenna elements. Nevertheless, the antenna element spacing is of half-wavelength or larger in [12], [13]. The capacity of spatially dense multiple antenna systems was pioneered in [14], which demonstrated that the capacity of such a system approaches a finite limit. The spatial DoF for sufficiently dense and large RISs have been studied in [6], and the achievable DoF for more common cases with finite element spacing and aperture areas has been investigated in [11], but the influence of channel conditions, such as the SNR, on the DoF has not been considered.

A. Contributions

In this paper, we consider wireless communications between two parallel RISs at the transmitter and receiver, respectively, and analyze the characteristics of eigenvalues of both the correlation matrix of an RIS and the composite channel matrix encompassing the two RISs and the wireless channel. The analysis herein differs from the existing literature in that a realistic, instead of assumed, spatial correlation model for RISs under isotropic scattering is employed, which has

been proven in [6], [10], [11]. The summations, individual behavior, and distributions of the eigenvalues are investigated for a plurality of RIS sizes and element spacing. Analytical forms are provided to characterize the eigenvalue distributions. Moreover, the effective degrees of freedom (EDoF), which denotes the number of subchannels actively conveying information [12], is studied and compared with the theoretical asymptotic DoF for sufficiently large and dense RISs without considering SNR conditions, in terms of their values and effect on channel capacity. Numerical results demonstrate that the EDoF relies on the operating SNR, in addition to spatial correlation which is in turn jointly determined by the physical parameters of RISs and propagation environment. The contributions in this paper are useful to channel estimation and beamforming design for RISs [15].

B. Outline of the Paper and Notation

The remainder of this paper is organized as follows. In Section II, we describe the system model containing RISs and identify the terms affecting the channel capacity. Asymptotic analysis of eigenvalues for both the correlation matrix at the RIS and the equivalent composite channel matrix is carried out in Section III. In Section IV, we systematically investigate the EDoF under various settings. Conclusions are drawn in Section V.

The following notations will be utilized throughout the paper: \mathbf{A} for matrix, \mathbf{a} for column vector, \mathbf{a}_k for the k th column of \mathbf{A} , $[\mathbf{A}]_{i,j}$ for the (i, j) th entry of \mathbf{A} , $\mathbf{a}_k(i)$ for the i th entry of \mathbf{a}_k , \mathbf{A}^H for transpose conjugate of \mathbf{A} , $\det(\mathbf{A})$ for determinant of the square matrix \mathbf{A} , $\text{tr}(\mathbf{A})$ for the trace of \mathbf{A} , and \mathbf{I}_N for the $N \times N$ identity matrix.

II. SYSTEM MODEL

We consider a point-to-point wireless communication system where the transmitter and receiver are each equipped with an RIS with N_T and N_R elements, respectively, where the two RISs are parallel with each other, as illustrated in Fig. 1. The horizontal and vertical lengths of the RISs are $L_{T,x}$, $L_{T,z}$ and $L_{R,x}$, $L_{R,z}$, respectively. For any subband of the radio bandwidth within which the channel response can be considered frequency-flat, the discrete-time system model is given by

$$\mathbf{y} = \sqrt{\rho}\mathbf{H}\mathbf{x} + \mathbf{n} \quad (1)$$

where $\mathbf{y} \in \mathbb{C}^{N_R \times 1}$, $\mathbf{H} \in \mathbb{C}^{N_R \times N_T}$, and $\mathbf{x} \in \mathbb{C}^{N_T \times 1}$ denote the received signal vector, channel matrix, and transmitted signal vector, respectively. ρ represents the signal-to-noise ratio (SNR) at the

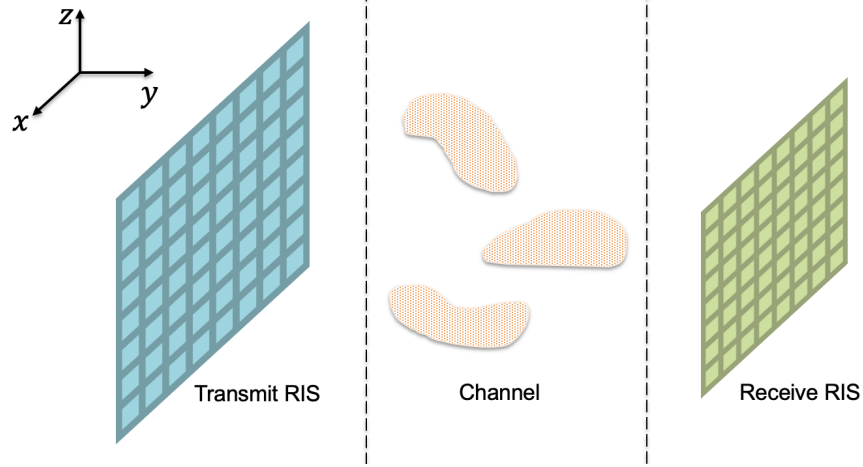


Fig. 1: Orientations of the transmit and receive RISs with respect to the associated coordinate system.

receiver that entails the large-scale fading coefficient. Besides, $\mathbf{n} \in \mathbb{C}^{N_R \times 1}$ represents the noise vector whose entries are independently and identically distributed (i.i.d.) circularly symmetric complex Gaussian random variables with mean zero. Owing to the compact arrangement of the elements in the RISs at both link ends, and the fact that the spatial correlation at each RIS is determined by the immediate surroundings to the RIS and not affected by the spatial correlation at the other end of the link in the far-field region [13], [16], [17], the spatial correlation matrices at the transmitter and receiver are separable. Therefore, \mathbf{H} can be factorized as [17], [18]

$$\mathbf{H} = \mathbf{R}_R^{1/2} \mathbf{H}_w \mathbf{R}_T^{1/2} \quad (2)$$

in which $\mathbf{R}_R \in \mathbb{C}^{N_R \times N_R}$ and $\mathbf{R}_T \in \mathbb{C}^{N_T \times N_T}$ are the correlation matrices at the receive and transmit RISs, respectively, while $\mathbf{H}_w \in \mathbb{C}^{N_R \times N_T}$ is i.i.d. Rayleigh-faded under isotropic scattering with the subscript w standing for "white". Denote the covariance matrix of the input signal vector \mathbf{x} as $\mathbf{Q} = \mathbb{E}\{\mathbf{x}\mathbf{x}^H\}$, the ergodic capacity of (1) in bit/s/Hz is [19]

$$C = \max_{\mathbf{Q}: \text{tr}(\mathbf{Q}) \leq 1} \mathbb{E} \left\{ \log_2 \det (\mathbf{I}_{N_R} + \rho \mathbf{H} \mathbf{Q} \mathbf{H}^H) \right\}. \quad (3)$$

With linear operations adopted at both the transmitter and receiver, (1) can be converted into an equivalent system involving N_S decoupled single-input single-output (SISO) subchannels, where each subchannel corresponds to a spatial eigenmode [12], and N_S satisfies

$$N_S \leq \min(N_T, N_R). \quad (4)$$

If assuming instantaneous channel state information (CSI) available at the receiver while no channel matrix information but just large-scale path loss available at the transmitter, which is one of the common scenarios in practice [12], the ergodic capacity in (3) is achieved by setting \mathbf{Q} as $\frac{1}{N_S}\mathbf{I}_{N_T}$, implying allocating the transmit power equally among the subchannels. Therefore, (3) is transformed to

$$C = \mathbb{E}\left\{\log_2 \det\left(\mathbf{I}_{N_R} + \frac{\rho}{N_S}\mathbf{H}\mathbf{H}^H\right)\right\} \quad (5)$$

It is worth noting that the uniform power allocation strategy does not require the knowledge of \mathbf{H} , rendering it appealing in a variety of systems where it is inconvenient or impossible to acquire the channel matrix. Plugging (2) into (5), we obtain

$$\begin{aligned} C &= \mathbb{E}\left\{\log_2 \det\left(\mathbf{I}_{N_R} + \frac{\rho}{N_S}\mathbf{R}_R^{1/2}\mathbf{H}_w\mathbf{R}_T^{1/2}\left(\mathbf{R}_R^{1/2}\mathbf{H}_w\mathbf{R}_T^{1/2}\right)^H\right)\right\} \\ &= \mathbb{E}\left\{\log_2 \det\left(\mathbf{I}_{N_R} + \frac{\rho}{N_S}\mathbf{R}_R\mathbf{H}_w\mathbf{R}_T\mathbf{H}_w^H\right)\right\} \end{aligned} \quad (6)$$

Since \mathbf{H}_w is isotropic, the distributions of $\mathbf{U}\mathbf{H}_w$ and $\mathbf{H}_w\mathbf{U}$ are identical to \mathbf{H}_w for any deterministic unitary matrix \mathbf{U} . Given that \mathbf{R}_T and \mathbf{R}_R are Hermitian, they can be decomposed as

$$\mathbf{R}_T = \mathbf{U}\mathbf{D}_T\mathbf{U}^H, \quad \mathbf{R}_R = \mathbf{V}\mathbf{D}_R\mathbf{V}^H \quad (7)$$

where $\mathbf{U} \in \mathbb{C}^{N_T \times N_T}$ and $\mathbf{V} \in \mathbb{C}^{N_R \times N_R}$ are unitary, while $\mathbf{D}_T \in \mathbb{C}^{N_T \times N_T}$ and $\mathbf{D}_R \in \mathbb{C}^{N_R \times N_R}$ are diagonal matrices composed of the eigenvalues of \mathbf{R}_T and \mathbf{R}_R , respectively, in non-increasing order. Combining (6) and (7) yields

$$\begin{aligned} C &= \mathbb{E}\left\{\log_2 \det\left(\mathbf{I}_{N_R} + \frac{\rho}{N_S}\mathbf{V}\mathbf{D}_R\mathbf{V}^H\mathbf{H}_w\mathbf{U}\mathbf{D}_T\mathbf{U}^H\mathbf{H}_w^H\right)\right\} \\ &= \mathbb{E}\left\{\log_2 \det\left(\mathbf{I}_{N_R} + \frac{\rho}{N_S}\mathbf{D}_R\mathbf{V}^H\mathbf{H}_w\mathbf{U}\mathbf{D}_T\mathbf{U}^H\mathbf{H}_w^H\mathbf{V}\right)\right\} \\ &\stackrel{\mathcal{D}}{=} \mathbb{E}\left\{\log_2 \det\left(\mathbf{I}_{N_R} + \frac{\rho}{N_S}\mathbf{D}_R\mathbf{H}_w\mathbf{D}_T\mathbf{H}_w^H\right)\right\} \end{aligned} \quad (8)$$

with \mathcal{D} meaning "in distribution". The third equation is by virtue of the fact that the entries of \mathbf{H}_w are i.i.d. complex Gaussian random variables, whose joint distribution will not change when \mathbf{H}_w is multiplied by a unitary matrix.

It is evident from (8) that the channel capacity is dependent on the eigenvalues of the random matrix $\mathbf{D}_R\mathbf{H}_w\mathbf{D}_T\mathbf{H}_w^H$ and an appropriate selection of N_S which are the core focus of this article. In the next section, we will first investigate the characteristics of the eigenvalues of \mathbf{R}_T and \mathbf{R}_R at the RISs, followed by the analysis on the asymptotic behavior of the eigenvalues of $\mathbf{D}_R\mathbf{H}_w\mathbf{D}_T\mathbf{H}_w^H$ and thus the capacity.

III. ASYMPTOTIC ANALYSIS OF EIGENVALUES

A. Characteristics of Eigenvalues of Correlation Matrix at the RIS

Substituting \mathbf{R}_T and \mathbf{R}_R in (2) with (7) results in

$$\mathbf{H} = \mathbf{V}\mathbf{D}_R^{1/2}\mathbf{V}^H\mathbf{H}_w\mathbf{U}\mathbf{D}_T^{1/2}\mathbf{U}^H = \mathbf{V}\mathbf{D}_R^{1/2}\tilde{\mathbf{H}}_w\mathbf{D}_T^{1/2}\mathbf{U}^H \quad (9)$$

where $\tilde{\mathbf{H}}_w = \mathbf{V}^H\mathbf{H}_w\mathbf{U} \in \mathbb{C}^{N_R \times N_T}$. Furthermore, denoting $\mathbf{D}_R^{1/2}\tilde{\mathbf{H}}_w\mathbf{D}_T^{1/2}$ as $\tilde{\mathbf{H}}$, we obtain

$$\mathbf{H} = \mathbf{V}\tilde{\mathbf{H}}\mathbf{U}^H \quad (10)$$

Employing the unitary property of \mathbf{V} and \mathbf{U} , (10) is tantamount to

$$\tilde{\mathbf{H}} = \mathbf{V}^H\mathbf{H}\mathbf{U} \quad (11)$$

which can be recast as

$$[\tilde{\mathbf{H}}]_{k,l} = \sum_{i=1}^{N_R} \sum_{j=1}^{N_T} \mathbf{v}_k^H(i) [\mathbf{H}]_{i,j} \mathbf{u}_l(j) \quad (12)$$

Since \mathbf{V} and \mathbf{U} are deterministic unitary matrices containing a set of complete orthonormal discrete basis functions formed by the eigenfunctions of \mathbf{R}_R and \mathbf{R}_T , respectively, $\tilde{\mathbf{H}}$ can be regarded as the Karhunen-Loeve transform (KLT) of \mathbf{H} [17]. $\{\mathbf{v}_k\}$ and $\{\mathbf{u}_l\}$ are the KLT kernel satisfying

$$\sum_{i'=1}^{N_R} [\mathbf{R}_R]_{i,i'} \mathbf{v}_k(i') = \alpha_k \mathbf{v}_k(i), \quad \sum_{j'=1}^{N_T} [\mathbf{R}_T]_{j,j'} \mathbf{u}_l(j') = \beta_l \mathbf{u}_l(j) \quad (13)$$

where α_k and β_l denote the k th eigenvalue of \mathbf{R}_R and l th eigenvalue of \mathbf{R}_T , respectively.

To investigate the features of the eigenvalues of \mathbf{R}_R and \mathbf{R}_T , let's focus on the transmitter side, since the receiver side can be treated similarly. For ease of exposition, we shall drop the subscript T by the following notations: $\mathbf{R} = \mathbf{R}_T$, $N = N_T$, $L_x = L_{T,x}$, and $L_z = L_{T,z}$. Without loss of generality, let $g(r)$, which maps $r \in [-\sqrt{L_x^2 + L_z^2}, \sqrt{L_x^2 + L_z^2}]$ to the real line, be the normalized (i.e., $g(0) = 1$) spatial correlation function for an RIS of fixed dimension, such that

$$g\left(\frac{i-j}{N-1}\sqrt{L_x^2 + L_z^2}\right) = \frac{[\mathbf{R}]_{i,j}}{N}, \quad i, j = 1, \dots, N \quad (14)$$

Let $\alpha_k^{\mathbf{A}}$ represent the k th largest eigenvalue of the matrix \mathbf{A} . Due to the normalization $g(0) = 1$, we have

$$\sum_{k=1}^N \alpha_k^{\mathbf{R}/N} = \text{tr}\left(\frac{\mathbf{R}}{N}\right) = 1, \quad \forall N \quad (15)$$

In addition, $\{\alpha_k^{(N)}\}$ will be converging to the point spectrum (i.e., eigenvalues) $\{\alpha_k^{(\infty)}\}$ of the non-negative definite Hermitian operator $\tilde{g}(x, y) = g((x - y)\sqrt{L_x^2 + L_z^2})$ where $x, y \in [0, 1]$ [14], [18]. $\{\alpha_k^{(\infty)}\}$ can be determined by

$$\int_0^1 g((x - y)\sqrt{L_x^2 + L_z^2})\phi_k(y)dy = \alpha_k^{(\infty)}\phi_k(x), \quad (16)$$

$$x \in [0, 1], k = 0, 1, \dots, \infty$$

in which $\{\phi_k(x)\}$ are the eigenfunctions of the operator $\tilde{g}(x, y)$. The nonzero eigenvalues of $\tilde{g}(x, y)$ have finite multiplicity and form a sequence approaching zero if they are denumerable infinite in number [18], [20]. Denote the number of nonzero eigenvalues of \mathbf{R}/N as $f(N)$, then $f(N) \sim o(N)$ [18]. Additionally, the speed of $f(N)/N \rightarrow 0$ relies on the smoothness of $g(r)$ in the sense of continuous differentiability of various orders, and smoother $g(r)$ gives rise to a more rapid convergence of $f(N)/N \rightarrow 0$.

It has been proven in [10], [11] that the spatial correlation matrix at an RIS under isotropic scattering can be characterized as a sinc function as follows

$$[\mathbf{R}]_{m,n} = \text{sinc}\left(\frac{2\|\mathbf{d}_m - \mathbf{d}_n\|}{\lambda}\right), \quad m, n = 1, \dots, N \quad (17)$$

where $\text{sinc}(x) = \frac{\sin(\pi x)}{\pi x}$ is the sinc function, \mathbf{d}_m and \mathbf{d}_n denote the coordinates of the m -th and n -th RIS element, respectively. The behavior of \mathbf{R} is depicted in Fig. 2 for element spacing up to four times the wavelength λ . It is observed from (17) and Fig. 2 that the spatial correlation is minimal only for some element spacing, instead of between any two elements, thus the i.i.d. Rayleigh fading model is not applicable in such a system [6], [10], [11].

Fig. 3 illustrates the eigenvalues of \mathbf{R}/N in non-increasing order for various N , or equivalently element spacing, with $L_x = L_z = 12\lambda$. Besides, the dotted vertical line represents the asymptotic spatial DoF $\lfloor \frac{\pi L_x L_z}{\lambda^2} \rfloor$ derived in [21] for $\min(L_x, L_z)/\lambda \rightarrow \infty$. To provide a more quantitative examination and comparison of the eigenvalues for different element spacing, some selected eigenvalues are listed in Table I. A few key remarks can be drawn from Fig. 3 and Table I: First, the i.i.d. Rayleigh fading channel has almost identical non-trivial eigenvalues whose amount equals the number of antenna elements deployed, while the correlated channel has uneven and fewer dominant eigenvalues and smaller rank. Second, as mentioned above, all the eigenvalues of \mathbf{R}/N converge for relatively large N , e.g., roughly starting from $d_x = d_z = \lambda/6$. Moreover, the dominant eigenvalues (whose indices are within around $\lfloor \frac{\pi L_x L_z}{\lambda^2} \rfloor$) converge even for small N corresponding to half-wavelength spacing. Additionally, as demonstrated in detail in [11], the

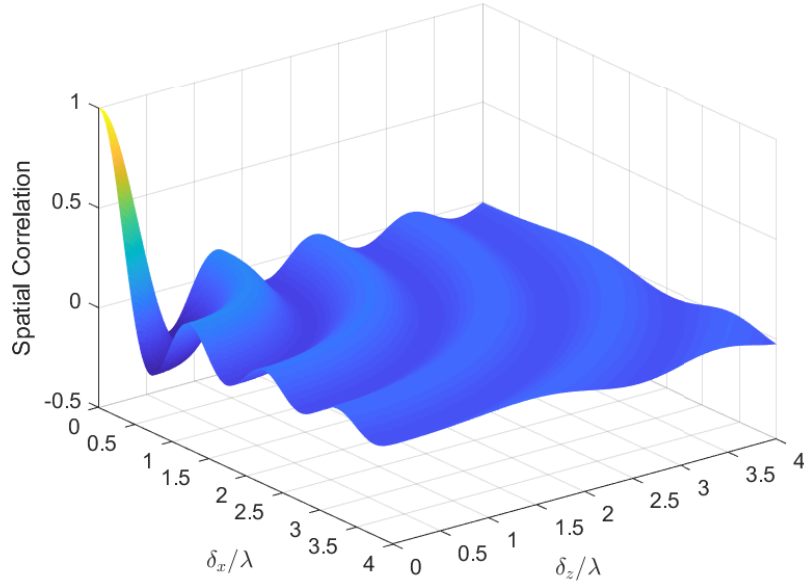


Fig. 2: Spatial correlation among RIS elements under isotropic scattering, where λ denotes the wavelength, δ_x/λ and δ_z/λ represent the element spacing along the x and z directions, respectively.

asymptotic spatial DoF $\lfloor \frac{\pi L_x L_z}{\lambda^2} \rfloor$ has non-negligible approximation errors for limited RIS aperture sizes which are often encountered in practice.

B. Characteristics of Eigenvalues of Channel Matrix

In this section, we study the eigenvalue behavior of the channel matrix $\mathbf{D}_R \mathbf{H}_w \mathbf{D}_T \mathbf{H}_w^H$ in (8). Define the matrix $\tilde{\mathbf{B}} \in \mathbb{C}^{N_R \times N_R}$ as the equivalent channel matrix normalized by the number of RIS elements at both the transmitter and receiver, i.e.

$$\tilde{\mathbf{B}} = \frac{\mathbf{D}_R \mathbf{H}_w \mathbf{D}_T \mathbf{H}_w^H}{N_T N_R} = \tilde{\mathbf{D}}_R \mathbf{H}_w \tilde{\mathbf{D}}_T \mathbf{H}_w^H. \quad (18)$$

where $\tilde{\mathbf{D}}_R = \mathbf{D}_R / N_R$ and $\tilde{\mathbf{D}}_T = \mathbf{D}_T / N_T$. It is relevant to first investigate the summation of the eigenvalues $\{\alpha_k^{\tilde{\mathbf{B}}}\}$ of $\tilde{\mathbf{B}}$. Note that

$$\sum_{k=1}^{N_R} \alpha_k^{\tilde{\mathbf{B}}} = \text{tr}(\tilde{\mathbf{B}}) = \sum_{i=1}^{N_R} [\tilde{\mathbf{B}}]_{i,i} \quad (19)$$

TABLE I: Selected eigenvalues of \mathbf{R}/N in non-increasing order for various element spacing d_x and d_z with $L_x = L_z = 12\lambda$

k	α_k				
	$d_x = d_z = \frac{\lambda}{2}$	$d_x = \frac{\lambda}{3}, d_z = \frac{\lambda}{2}$	$d_x = d_z = \frac{\lambda}{4}$	$d_x = d_z = \frac{\lambda}{6}$	$d_x = d_z = \frac{\lambda}{12}$
1	0.00679	0.00688	0.00479	0.00484	0.00489
2	0.00679	0.00663	0.00479	0.00484	0.00489
3	0.00655	0.00620	0.00479	0.00483	0.00488
4	0.00655	0.00557	0.00479	0.00483	0.00488
5	0.00614	0.00479	0.00457	0.00461	0.00466
6	0.00614	0.00471	0.00457	0.00461	0.00466
7	0.00554	0.00471	0.00457	0.00461	0.00466
8	0.00554	0.00469	0.00457	0.00461	0.00466
9	0.00479	0.00469	0.00450	0.00454	0.00459
10	0.00478	0.00466	0.00450	0.00454	0.00458
50	0.00380	0.00393	0.00412	0.00415	0.00418
100	0.00245	0.00242	0.00242	0.00244	0.00246
200	0.00169	0.00171	0.00173	0.00172	0.00172
300	0.00137	0.00138	0.00141	0.00142	0.00143
400	0.00117	0.00118	0.00119	0.00120	0.00121
500	0.00104	0.00105	0.00099	0.00087	0.00075
600	1.24×10^{-8}	6.82×10^{-6}	2.23×10^{-5}	1.93×10^{-5}	1.56×10^{-5}
700	N/A	6.05×10^{-10}	1.82×10^{-7}	2.12×10^{-7}	1.87×10^{-7}
800	N/A	2.97×10^{-15}	1.08×10^{-9}	1.66×10^{-9}	1.64×10^{-9}
900	N/A	0	4.16×10^{-12}	9.88×10^{-12}	1.13×10^{-11}
1000	N/A	N/A	1.40×10^{-14}	5.19×10^{-14}	7.47×10^{-14}
2000	N/A	N/A	0	1.05×10^{-18}	1.41×10^{-18}
3000	N/A	N/A	N/A	2.11×10^{-19}	1.08×10^{-18}

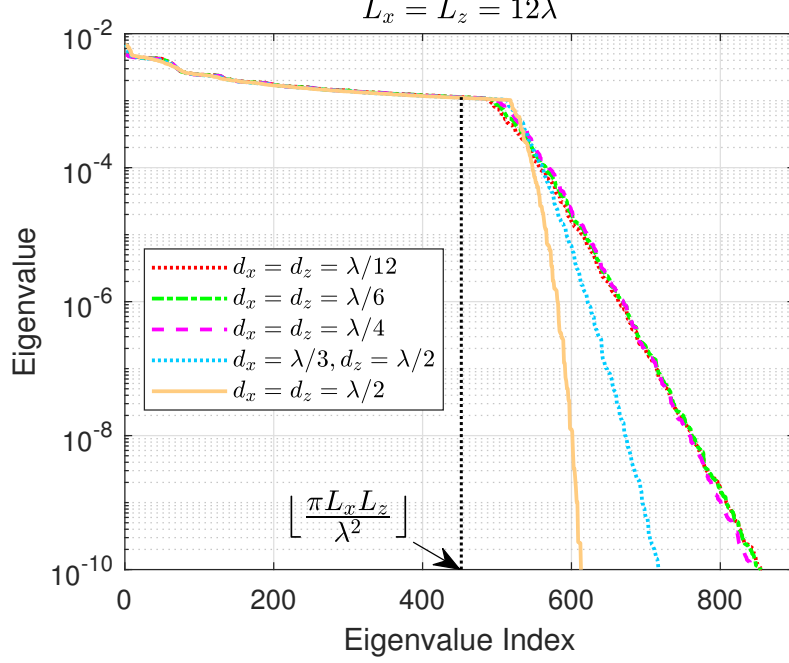


Fig. 3: Eigenvalues of \mathbf{R}/N in non-increasing order for various element spacing d_x and d_z with $L_x = L_z = 12\lambda$. Also depicted is the asymptotic spatial degrees of freedom (DoF) $\lfloor \frac{\pi L_x L_z}{\lambda^2} \rfloor$ derived in [21] for $\min(L_x, L_z)/\lambda \rightarrow \infty$.

where $[\tilde{\mathbf{B}}]_{i,i}$ is calculated as

$$\begin{aligned}
 [\tilde{\mathbf{B}}]_{i,i} &= [\tilde{\mathbf{D}}_{\mathbf{R}}]_{i,i} \sum_{l=1}^{N_{\mathbf{T}}} |[\mathbf{H}_w]_{i,l}|^2 [\tilde{\mathbf{D}}_{\mathbf{T}}]_{l,l} \\
 &\stackrel{(a)}{\approx} [\tilde{\mathbf{D}}_{\mathbf{R}}]_{i,i} \sum_{l=1}^{N_{\mathbf{T}}} [\tilde{\mathbf{D}}_{\mathbf{T}}]_{l,l} \\
 &\stackrel{(b)}{=} [\tilde{\mathbf{D}}_{\mathbf{R}}]_{i,i}
 \end{aligned} \tag{20}$$

where (a) is because the variance of each element in \mathbf{H}_w is 1, and (b) is ascribed to the normalized eigenvalue summation of $\mathbf{R}_{\mathbf{T}}/N_{\mathbf{T}}$ as shown in (15). Plugging (20) into (19) gives

$$\sum_{k=1}^{N_{\mathbf{R}}} \alpha_k^{\tilde{\mathbf{B}}} \approx \sum_{i=1}^{N_{\mathbf{R}}} [\tilde{\mathbf{D}}_{\mathbf{R}}]_{i,i} = 1 \tag{21}$$

which proves that the summation of the eigenvalues of $\tilde{\mathbf{B}}$ is approximately 1 which equals the respective eigenvalue summation of $\mathbf{R}_{\mathbf{T}}/N_{\mathbf{T}}$ and $\mathbf{R}_{\mathbf{R}}/N_{\mathbf{R}}$. The cumulative distribution function

(CDF) $F(\alpha^{\tilde{\mathbf{B}}})$ of an arbitrary unordered eigenvalue of $\tilde{\mathbf{B}}$ can be derived from the result in [22, (15)], which is expressed as

$$F(\alpha^{\tilde{\mathbf{B}}}) = \frac{1}{N_{\text{R}}} - \frac{Q_0(\alpha^{\tilde{\mathbf{B}}})R_0}{N_{\text{T}}N_{\text{R}}} \sum_{n=1}^{N_{\text{R}}} \det \left(\left[\mathbf{K}^{(n)} \right]_{i,j} \right) \quad (22)$$

where

$$Q_v(z)^{-1} = \Delta_{N_{\text{R}}}(\alpha^{\tilde{\mathbf{D}}_{\text{R}}}) \Delta_{N_{\text{T}}}(\alpha^{\tilde{\mathbf{D}}_{\text{T}}}) (-z)^{N_{\text{T}}(N_{\text{T}}-1)/2} J_v \quad (23)$$

in which Δ represents a V -dimensional Vandermonde determinant given by

$$\Delta_V(x) = \prod_{1 \leq i < j \leq V} (x_j - x_i) = \det [x_j^{i-1}] \quad (24)$$

and J_v is calculated as

$$J_v = \prod_{i=1}^{N_{\text{R}}-1} (v+i)^i \quad (25)$$

R_v in (22) is defined as

$$R_v = \begin{cases} \prod_{j=1}^{N_{\text{R}}-N_{\text{T}}-1} (N_{\text{R}}+v-j)^{N_{\text{R}}-N_{\text{T}}-j}, & N_{\text{R}} > N_{\text{T}} + 1 \\ 1, & N_{\text{R}} \leq N_{\text{T}} + 1 \end{cases} \quad (26)$$

The $N_{\text{R}} \times N_{\text{R}}$ matrix $\mathbf{K}^{(n)}$ in (22) is given by

$$\left[\mathbf{K}^{(n)} \right]_{i,j} = \begin{cases} g(\alpha_i^{\tilde{\mathbf{D}}_{\text{R}}} \alpha_j^{\tilde{\mathbf{D}}_{\text{T}}}; N_{\text{R}}, \alpha^{\tilde{\mathbf{B}}}), & n \neq i \\ (N_{\text{R}} - 1)! e^{-\alpha_i^{\tilde{\mathbf{D}}_{\text{R}}} \alpha_j^{\tilde{\mathbf{D}}_{\text{T}}} \alpha^{\tilde{\mathbf{B}}}}, & n = i \end{cases} \quad (27)$$

in which for integer $M > 0$, the function g is defined as [22, (13)]

$$g(x; M, z) = x^{N_{\text{R}}-M} (M-1)! \sum_{m=0}^{M-1} \frac{(-zx)^m}{m!} \quad (28)$$

Next, we explore the behavior of individual eigenvalues of $\tilde{\mathbf{B}}$ in (18), and start with the matrix without the term \mathbf{D}_{R} in $\tilde{\mathbf{B}}$, i.e.

$$\mathbf{F} = \frac{\mathbf{H}_w \mathbf{D}_{\text{T}} \mathbf{H}_w^{\text{H}}}{N_{\text{T}} N_{\text{R}}} = \frac{1}{N_{\text{R}}} \mathbf{H}_w \tilde{\mathbf{D}}_{\text{T}} \mathbf{H}_w^{\text{H}} \quad (29)$$

which yields

$$\alpha_k^{\mathbf{F}} = \alpha_k^{\frac{1}{N_{\text{R}}} \mathbf{H}_w \tilde{\mathbf{D}}_{\text{T}} \mathbf{H}_w^{\text{H}}} = \alpha_k^{\frac{1}{N_{\text{R}}} \mathbf{H}_w^{\text{H}} \mathbf{H}_w \tilde{\mathbf{D}}_{\text{T}}}, \quad k = 1, \dots, \text{rank}(\mathbf{F}) \quad (30)$$

where the second equality stems from the fact that the (nonzero) eigenvalues of the matrix \mathbf{AB} equal those of \mathbf{BA} (with qualifying dimensions of \mathbf{A} and \mathbf{B}). It has been proved in [23] that for a matrix with the form $\frac{1}{N_R} \mathbf{H}_w^H \mathbf{H}_w \tilde{\mathbf{D}}_T$ in (30), the following inequality holds:

$$\alpha_k^{\tilde{\mathbf{D}}_T} \alpha_{\text{rank}(\mathbf{F})}^{\frac{1}{N_R} \mathbf{H}_w^H \mathbf{H}_w} \leq \alpha_k^{\mathbf{F}} \leq \alpha_k^{\tilde{\mathbf{D}}_T} \alpha_1^{\frac{1}{N_R} \mathbf{H}_w^H \mathbf{H}_w}, \quad k = 1, \dots, \text{rank}(\mathbf{F}) \quad (31)$$

where $\alpha_{\text{rank}(\mathbf{F})}^{\frac{1}{N_R} \mathbf{H}_w^H \mathbf{H}_w}$ and $\alpha_1^{\frac{1}{N_R} \mathbf{H}_w^H \mathbf{H}_w}$ are the smallest and largest eigenvalues of the uncorrelated central complex Wishart matrix $\frac{1}{N_R} \mathbf{H}_w^H \mathbf{H}_w$ [19], [24], respectively, which satisfy the following properties [23], [25]

$$\alpha_1^{\frac{1}{N_R} \mathbf{H}_w^H \mathbf{H}_w} \xrightarrow{\text{a.s.}} (1 + \sqrt{\eta})^2, \quad \alpha_{\text{rank}(\mathbf{F})}^{\frac{1}{N_R} \mathbf{H}_w^H \mathbf{H}_w} \xrightarrow{\text{a.s.}} (1 - \sqrt{\eta})^2 \quad (32)$$

in which "a.s." means almost sure, and $\eta = N_T/N_R$. We briefly analyze three conditions in terms of η : (1) If $N_T \ll N_R$ ($\eta \rightarrow 0$), from the law of large numbers, the eigenvalues of \mathbf{F} in (29) converge to those in $\tilde{\mathbf{D}}_T$ pointwisely with high probability; (2) If $N_T \gg N_R$ ($\eta \gg 1$), $\alpha_k^{\mathbf{F}} \approx \eta \alpha_k^{\tilde{\mathbf{D}}_T}$; (3) If $N_T \approx N_R$ ($\eta \approx 1$), $0 \lesssim \alpha_k^{\mathbf{F}} \lesssim 4\alpha_k^{\tilde{\mathbf{D}}_T}$.

With the observation above at hand, we now investigate the eigenvalue characteristics of $\tilde{\mathbf{B}}$ in (18) that can be rewritten as

$$\tilde{\mathbf{B}} = \mathbf{D}_R \mathbf{F} = N_R \tilde{\mathbf{D}}_R \mathbf{F} \quad (33)$$

where $\tilde{\mathbf{D}}_R = \mathbf{D}_R/N_R$ whose eigenvalue properties have been studied in Section III-A. Since \mathbf{F} in (29) is Hermitian, the condition below holds for positive eigenvalues in $\tilde{\mathbf{D}}_R$ and non-negative eigenvalues of \mathbf{F} [26, Theorem 2.2]:

$$N_R \alpha_k^{\mathbf{F}} \alpha_{\text{rank}(\tilde{\mathbf{D}}_R)}^{\tilde{\mathbf{D}}_R} \leq \alpha_k^{\tilde{\mathbf{B}}} \leq N_R \alpha_k^{\mathbf{F}} \alpha_1^{\tilde{\mathbf{D}}_R}. \quad (34)$$

Combining (31), (32), and (34), the following can be concluded:

$$\begin{aligned} N_R \alpha_k^{\tilde{\mathbf{D}}_T} \alpha_{\text{rank}(\tilde{\mathbf{D}}_R)}^{\tilde{\mathbf{D}}_R} &\lesssim \alpha_k^{\tilde{\mathbf{B}}} \lesssim N_R \alpha_k^{\tilde{\mathbf{D}}_T} \alpha_1^{\tilde{\mathbf{D}}_R}, \quad \text{if } N_T \ll N_R, \\ N_T \alpha_k^{\tilde{\mathbf{D}}_T} \alpha_{\text{rank}(\tilde{\mathbf{D}}_R)}^{\tilde{\mathbf{D}}_R} &\lesssim \alpha_k^{\tilde{\mathbf{B}}} \lesssim N_T \alpha_k^{\tilde{\mathbf{D}}_T} \alpha_1^{\tilde{\mathbf{D}}_R}, \quad \text{if } N_T \gg N_R, \\ 0 &\lesssim \alpha_k^{\tilde{\mathbf{B}}} \lesssim 4N_R \alpha_k^{\tilde{\mathbf{D}}_T} \alpha_1^{\tilde{\mathbf{D}}_R}, \quad \text{if } N_T \approx N_R. \end{aligned} \quad (35)$$

Note that the roles of \mathbf{D}_T and \mathbf{D}_R in (18) are actually equivalent, thus (29)-(35) still hold if swapping the subscripts T and R in them. Consequently, (35) can be extended to (36). Since the lower and upper bounds of $\alpha_k^{\tilde{\mathbf{B}}}$ in (36) are relatively loose, Monte Carlo simulations are performed to allow for more intuitive understanding. The simulation condition is $N_T = N_R$ and

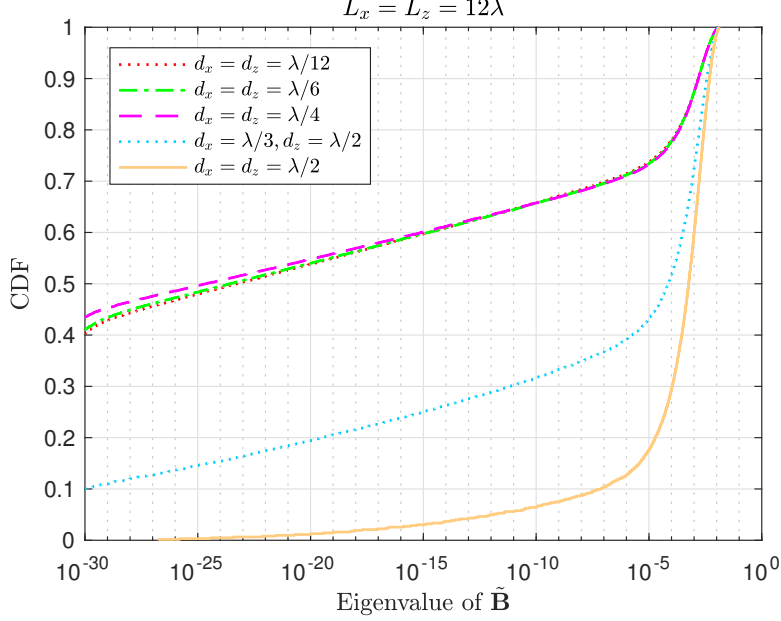


Fig. 4: CDF of the eigenvalues of $\tilde{\mathbf{B}}$ for various element spacing d_x and d_z with $L_x = L_z = 12\lambda$.

$$\begin{aligned}
 \max(N_R \alpha_k^{\tilde{\mathbf{D}}_T} \alpha_{\text{rank}(\tilde{\mathbf{D}}_R)}^{\tilde{\mathbf{D}}_R}, N_R \alpha_k^{\tilde{\mathbf{D}}_R} \alpha_{\text{rank}(\tilde{\mathbf{D}}_T)}^{\tilde{\mathbf{D}}_T}) &\lesssim \alpha_k^{\tilde{\mathbf{B}}} \lesssim \min(N_R \alpha_k^{\tilde{\mathbf{D}}_T} \alpha_1^{\tilde{\mathbf{D}}_R}, N_R \alpha_k^{\tilde{\mathbf{D}}_R} \alpha_1^{\tilde{\mathbf{D}}_T}), \text{ if } N_T \ll N_R, \\
 \max(N_T \alpha_k^{\tilde{\mathbf{D}}_T} \alpha_{\text{rank}(\tilde{\mathbf{D}}_R)}^{\tilde{\mathbf{D}}_R}, N_T \alpha_k^{\tilde{\mathbf{D}}_R} \alpha_{\text{rank}(\tilde{\mathbf{D}}_T)}^{\tilde{\mathbf{D}}_T}) &\lesssim \alpha_k^{\tilde{\mathbf{B}}} \lesssim \min(N_T \alpha_k^{\tilde{\mathbf{D}}_T} \alpha_1^{\tilde{\mathbf{D}}_R}, N_T \alpha_k^{\tilde{\mathbf{D}}_R} \alpha_1^{\tilde{\mathbf{D}}_T}), \text{ if } N_T \gg N_R, \\
 0 &\lesssim \alpha_k^{\tilde{\mathbf{B}}} \lesssim \min(4N_R \alpha_k^{\tilde{\mathbf{D}}_T} \alpha_1^{\tilde{\mathbf{D}}_R}, 4N_T \alpha_k^{\tilde{\mathbf{D}}_R} \alpha_1^{\tilde{\mathbf{D}}_T}), \text{ if } N_T \approx N_R.
 \end{aligned} \tag{36}$$

the RISs at the transmitter and receiver have the same dimensions, as this case renders it the most difficult to obtain tight analytical bounds on individual eigenvalues of the channel.

Under the condition of $N_T = N_R = N$, the CDF $F(\alpha^{\tilde{\mathbf{B}}})$ in (22) can be simplified to

$$F(\alpha^{\tilde{\mathbf{B}}}) = \frac{1}{N} - \frac{Q_0(\alpha^{\tilde{\mathbf{B}}})}{N^2} \sum_{n=1}^N \det\left(\left[\mathbf{K}^{(n)}\right]_{i,j}\right) \tag{37}$$

$F(\alpha^{\tilde{\mathbf{B}}})$ is illustrated in Fig. 4 for various element spacing d_x and d_z which results in different values of N , with $L_x = L_z = 12\lambda$ as an example.

Fig. 5 depicts the probability density distributions (PDFs) of the first 12 largest eigenvalues of $\tilde{\mathbf{B}}$ in (18) with $L_x = L_z = 12\lambda$ and $d_x = d_z = \lambda/12$, obtained from 1000 random realizations of \mathbf{H}_w . The mean μ and standard deviation σ via fitting using the Gaussian distribution are also

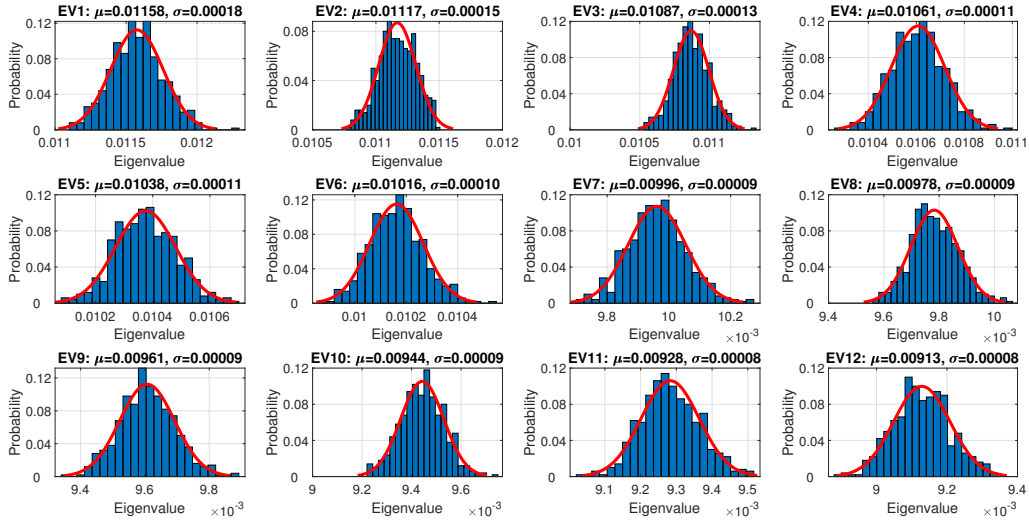


Fig. 5: Probability density distributions (PDFs) of the first 12 largest eigenvalues of $\tilde{\mathbf{B}}$ in (18) with $L_x = L_z = 12\lambda$ and $d_x = d_z = \lambda/12$.

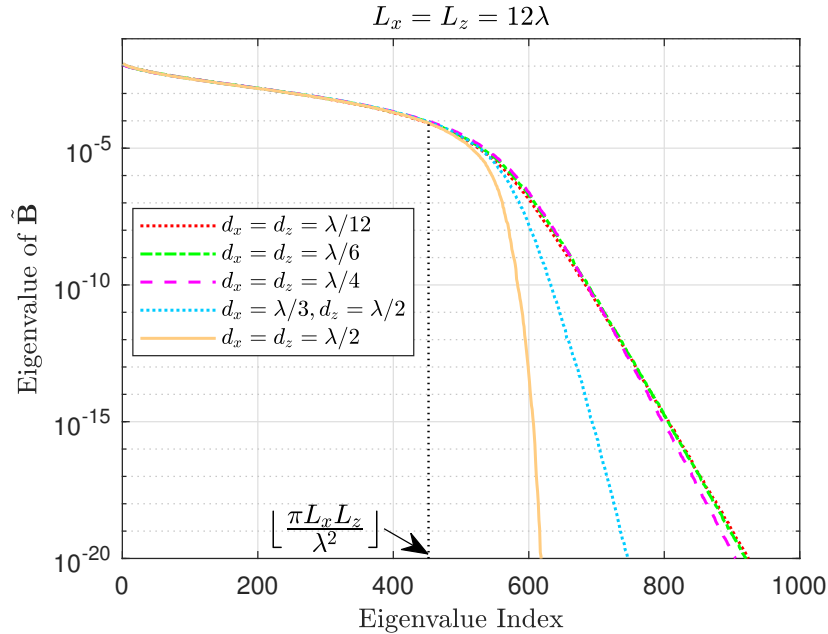


Fig. 6: Eigenvalues of $\tilde{\mathbf{B}}$ in (18) in non-increasing order for various element spacing d_x and d_z with $L_x = L_z = 12\lambda$. Also depicted is the asymptotic spatial degrees of freedom (DoF) $\lfloor \frac{\pi L_x L_z}{\lambda^2} \rfloor$ derived in [21] for $\min(L_x, L_z)/\lambda \rightarrow \infty$.

displayed for each PDF. It is evident based on the tiny standard deviations that each of the eigenvalues well obey the normal distribution with a large concentration around the mean value. Fig. 6 shows the eigenvalues of $\tilde{\mathbf{B}}$ in (18) with the same RIS dimensions and element spacing in Fig. 3, where each curve is averaged over 1000 random realizations of \mathbf{H}_w . Some selected eigenvalues of $\tilde{\mathbf{B}}$ are listed in Table II to provide a more quantitative demonstration.

IV. EFFECTIVE DEGREES OF FREEDOM

For ease of exposition, denote the sequence of the eigenvalues of $\tilde{\mathbf{B}}$ in (18) as $\{\gamma_k\}$. When $N_T \leq N_R$, and instantaneous CSI is only available at the receiver which is usually the case in practice, the channel capacity in (8) can be recast as [12]

$$C = \sum_{k=1}^{N_S} \mathbb{E} \left\{ \log_2 \left(1 + \frac{\rho N_T N_R}{N_S} \gamma_k \right) \right\}. \quad (38)$$

where N_S is given in (4) and the text above it. To analyze the EDoF with which the capacity is maximized, an asymptotic continuous function relevant to C in (38) is defined as follows

$$h(N_S) = \int_1^{N_S} \log_2 \left(1 + \frac{\rho N_T N_R}{N_S} \gamma(x) \right) dx \quad (39)$$

where $h(N_S)$ is a continuous function of N_S , and $\gamma(x)$ represents the continuous counterpart of $\{\gamma_k\}$ as illustrated in Fig. 6. Comparing Figs. 4 and 6, it is observed that for the same L_x , L_z , and N (or equivalently element spacing d_x and d_z), the eigenvalues $\gamma(x)$ in Fig. 6 and the CDF $F(\alpha^{\tilde{\mathbf{B}}})$ in Fig. 4 can be related as follows:

$$\gamma(x) = F^{-1} \left(1 - \frac{x}{N} \right) \quad (40)$$

where $F^{-1}(\cdot)$ denotes the inverse function of the CDF $F(\cdot)$ in (37). The EDoF N_S^* maximizing the capacity satisfies

$$\left. \frac{dh(N_S)}{dN_S} \right|_{N_S=N_S^*} = 0. \quad (41)$$

Employing (39) and the Leibniz integral rule [27], $\frac{dh(N_S)}{dN_S}$ is given by (42), where the analytical form of $\gamma(x)$ is provided in (40).

$$\begin{aligned} \frac{dh(N_S)}{dN_S} &= \log_2 \left(1 + \frac{\rho N_T N_R}{N_S} \gamma(N_S) \right) + \frac{1}{\log 2} \int_1^{N_S} \left[\frac{1}{1 + \frac{\rho N_T N_R}{N_S} \gamma(x)} \times \left(-\frac{\rho N_T N_R}{N_S^2} \gamma(x) \right) \right] dx \\ &= \log_2 \left(1 + \frac{\rho N_T N_R}{N_S} \gamma(N_S) \right) - \frac{1}{N_S \log 2} \int_1^{N_S} \frac{\frac{\rho N_T N_R}{N_S} \gamma(x)}{1 + \frac{\rho N_T N_R}{N_S} \gamma(x)} dx \end{aligned} \quad (42)$$

TABLE II: Selected eigenvalues of $\tilde{\mathbf{B}}$ in non-increasing order for various element spacing d_x and d_z with $L_x = L_z = 12\lambda$

k	$\alpha_k^{\tilde{\mathbf{B}}}$				
	$d_x = d_z = \frac{\lambda}{2}$	$d_x = \frac{\lambda}{3}, d_z = \frac{\lambda}{2}$	$d_x = d_z = \frac{\lambda}{4}$	$d_x = d_z = \frac{\lambda}{6}$	$d_x = d_z = \frac{\lambda}{12}$
1	0.01268	0.01216	0.01134	0.01148	0.01158
2	0.01210	0.01154	0.01095	0.01107	0.01115
3	0.01162	0.01114	0.01066	0.01076	0.01086
4	0.01126	0.01081	0.01040	0.01051	0.01061
5	0.01091	0.01051	0.01018	0.01029	0.01038
6	0.01062	0.01025	0.00998	0.01006	0.01017
7	0.01038	0.01003	0.00978	0.00988	0.00997
8	0.01013	0.00980	0.00960	0.00970	0.00978
9	0.00991	0.00961	0.00943	0.00954	0.00962
10	0.00971	0.00942	0.00927	0.00937	0.00945
50	0.00551	0.00554	0.00557	0.00560	0.00561
100	0.00334	0.00346	0.00348	0.00347	0.00348
200	0.00153	0.00155	0.00158	0.00156	0.00155
300	0.00069	0.00068	0.00068	0.00065	0.00065
400	0.00023	0.00022	0.00023	0.00021	0.00020
500	2.70×10^{-5}	2.73×10^{-5}	3.18×10^{-5}	2.83×10^{-5}	2.46×10^{-5}
600	5.61×10^{-14}	1.58×10^{-8}	2.41×10^{-7}	1.96×10^{-7}	1.37×10^{-7}
700	N/A	2.73×10^{-16}	2.46×10^{-11}	2.91×10^{-11}	2.23×10^{-11}
800	N/A	7.84×10^{-27}	8.27×10^{-16}	1.75×10^{-15}	1.77×10^{-15}
900	N/A	0	1.69×10^{-20}	7.83×10^{-20}	1.10×10^{-19}
1000	N/A	N/A	2.47×10^{-25}	2.85×10^{-24}	5.80×10^{-24}
2000	N/A	N/A	0	0	0
3000	N/A	N/A	N/A	0	0

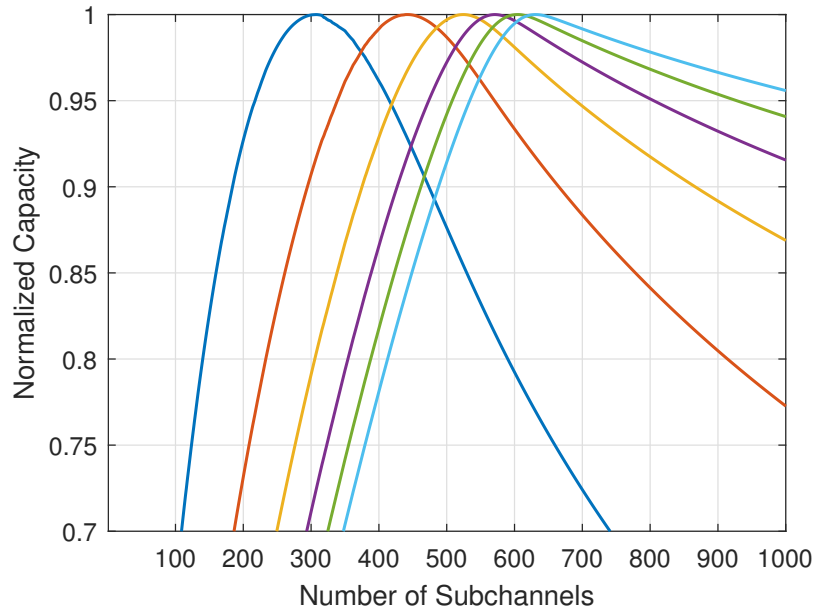


Fig. 7: Normalized capacity versus number of subchannels on which data is sent, with $L_x = L_z = 12\lambda$ and $d_x = d_z = \lambda/4$. The curves from leftmost to rightmost represent receive SNRs of -10 dB to 40 dB in increments of 10 dB, respectively.

It is straightforward from (41) and (42) that the EDoF N_S^* must satisfy

$$\log_2 \left(1 + \frac{\rho N_T N_R}{N_S^*} \gamma(N_S^*) \right) = \frac{1}{N_S^* \log 2} \int_1^{N_S^*} \frac{\frac{\rho N_T N_R}{N_S^*} \gamma(x)}{1 + \frac{\rho N_T N_R}{N_S^*} \gamma(x)} dx \quad (43)$$

It is evident from (43) that the EDoF N_S^* relies upon not only the eigenvalue distribution of the normalized equivalent channel $\tilde{\mathbf{B}}$ in (18), but also the SNR ρ at the receiver as well as $N_T N_R$. Although analytical expressions of all the terms in (43) have been obtained, it is still difficult to derive a closed-form expression of N_S^* due to the extremely complicated form of $\gamma(x)$ in (40). Therefore, we resort to numerical simulations to unveil the behavior of N_S^* under a variety of conditions.

Fig. 7 displays the normalized capacity versus number of subchannels on which data is sent, with $L_x = L_z = 12\lambda$ and $d_x = d_z = \lambda/4$. The curves from leftmost to rightmost represent receive SNRs of -10 dB to 40 dB in increments of 10 dB, respectively. It is obvious from Fig. 7 that the capacity reaches its maximum value at different numbers of subchannels as the receive SNR changes, indicating that the optimal number of subchannels, i.e., the EDoF, is not fixed for given RIS configurations but varies with channel conditions, as expected and validated in

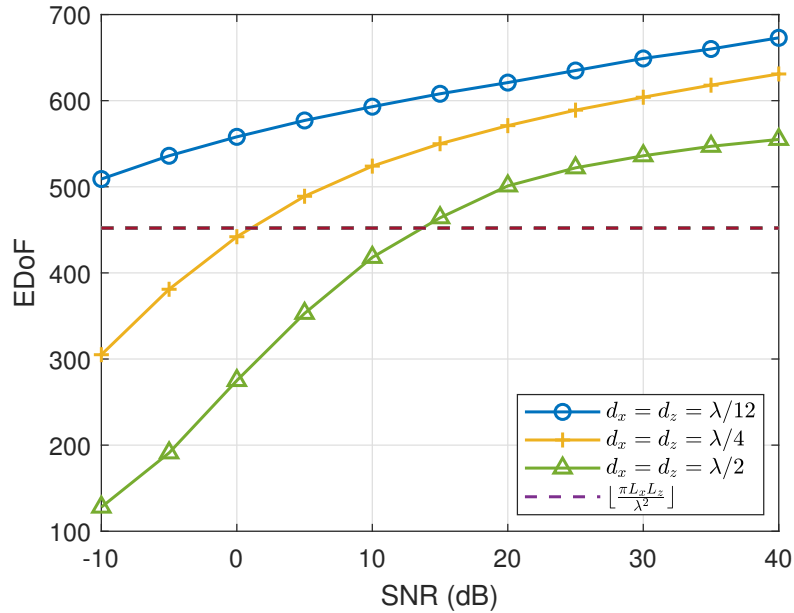


Fig. 8: Effective degrees of freedom (EDoF) as a function of receive SNR for various element spacing d_x and d_z with $L_x = L_z = 12\lambda$. The dashed straight line limns the asymptotic spatial degrees of freedom (DoF) $\lfloor \frac{\pi L_x L_z}{\lambda^2} \rfloor$ without considering SNR conditions.

practice [12], [28]. To provide a more explicit comparison on the EDoF and the DoF $\lfloor \frac{\pi L_x L_z}{\lambda^2} \rfloor$ without considering the SNR condition, we show the EDoF as a function of receive SNR for various element spacing d_x and d_z with $L_x = L_z = 12\lambda$ in Fig. 8, from which the following remarks can be made: First, for a given number of RIS elements N or element spacing d_x and d_z , the EDoF alters with SNR in a non-linear manner. Second, the the alteration rate and range of EDoF change with element spacing d_x and d_z . Third, the EDoF can be smaller than, equal to, or larger than the SNR-unaware DoF $\lfloor \frac{\pi L_x L_z}{\lambda^2} \rfloor$ [11], [21], depending on the element spacing d_x and d_z along with SNR. This implies that the DoF $\lfloor \frac{\pi L_x L_z}{\lambda^2} \rfloor$ is not necessarily the upper bound of the EDoF. Moreover, the difference between EDoF and the SNR-unaware DoF can be huge (e.g., one can be twice of the other in some cases).

The impact of DoF on capacity is illustrated in Fig. 9 for various element spacing d_x and d_z with $L_x = L_z = 12\lambda$, where the upper plot shows the capacity versus receive SNR for both EDoF and the DoF $\lfloor \frac{\pi L_x L_z}{\lambda^2} \rfloor$, and the lower plot depicts the capacity degradation of using the DoF $\lfloor \frac{\pi L_x L_z}{\lambda^2} \rfloor$ against the EDoF. As is seen, the maximum capacity degradation can reach about 40% if sending data on the conventional $\lfloor \frac{\pi L_x L_z}{\lambda^2} \rfloor$ subchannels as opposed to the optimal

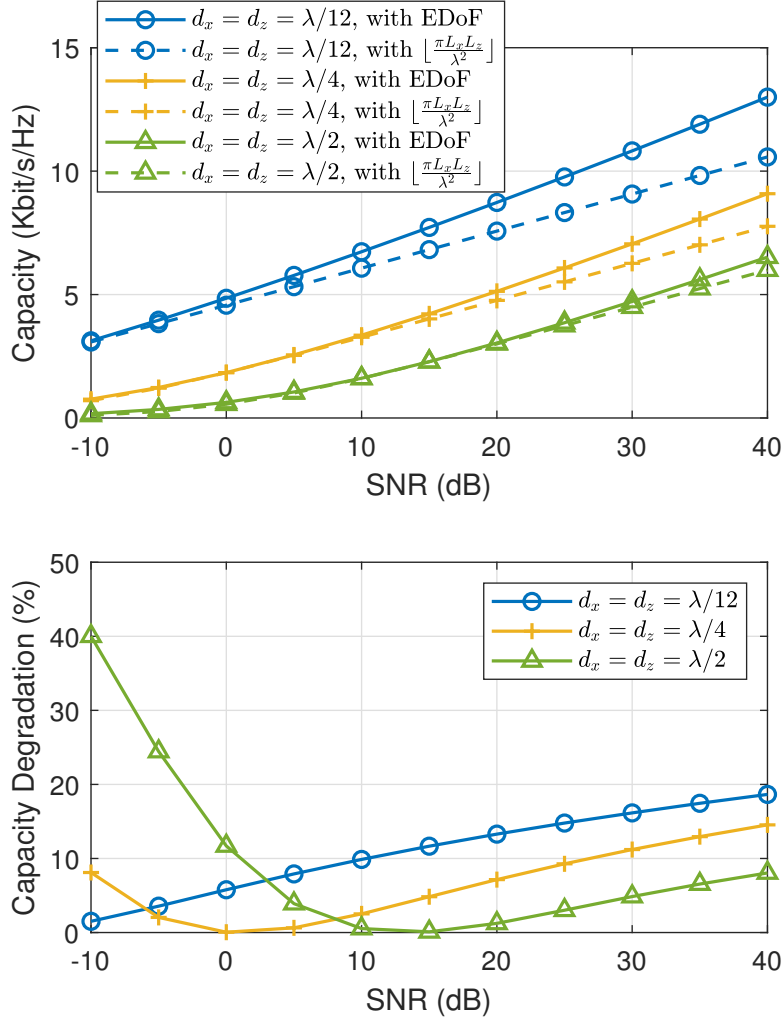


Fig. 9: Upper: Capacity versus receive SNR for both EDoF and the DoF $\lfloor \frac{\pi L_x L_z}{\lambda^2} \rfloor$ for various element spacing d_x and d_z with $L_x = L_z = 12\lambda$. Lower: Capacity degradation of using the DoF $\lfloor \frac{\pi L_x L_z}{\lambda^2} \rfloor$ against the EDoF for various element spacing d_x and d_z with $L_x = L_z = 12\lambda$.

number of subchannels represented by EDoF. The analysis above shows that the effective optimal number of subchannels, or equivalently spatial eigenmodes, is not solely determined by the spatial correlation of the RISs, but also by how many spatial eigenmodes are “illuminated” by the transmit power after the weakening by large-scale fading and noise.

To gain insights on how the EDoF and capacity behaves with different L_x and L_z , similar simulations are performed for $L_x = L_z = 32\lambda$, whose results are demonstrated in Figs. 10 and 11. It is observed from that the discrepancy between EDoF and the SNR-unaware DoF

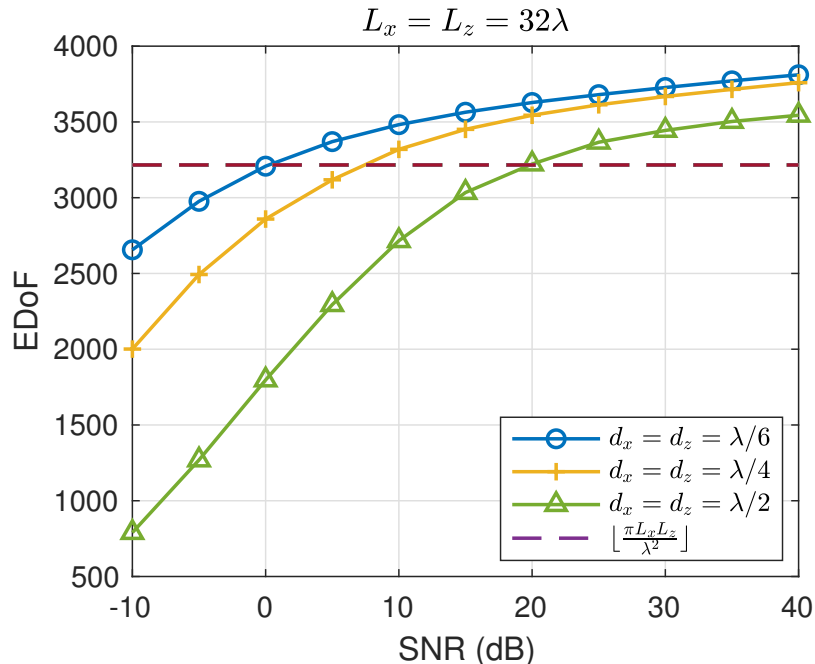


Fig. 10: Effective degrees of freedom (EDoF) as a function of receive SNR for various element spacing d_x and d_z with $L_x = L_z = 32\lambda$. The dashed straight line limits the asymptotic spatial degrees of freedom (DoF) $\lfloor \frac{\pi L_x L_z}{\lambda^2} \rfloor$ without considering SNR conditions.

$\lfloor \frac{\pi L_x L_z}{\lambda^2} \rfloor$ and the capacity degradation decrease at moderate to high SNRs, but become even more prominent at low SNRs, as compared to smaller L_x and L_z in Figs. 8 and 9. This can be explained by the fact that as L_x/λ and L_z/λ increase, the accuracy of the asymptotic DoF $\lfloor \frac{\pi L_x L_z}{\lambda^2} \rfloor$ also ascends, such that the EDoF is close to $\lfloor \frac{\pi L_x L_z}{\lambda^2} \rfloor$ as long as the SNR is not too low, i.e., the spatial eigenmodes are sufficiently “illuminated”. On the other hand, the power allocated to the weak eigenmodes is very poorly used, thus the DoF error is enlarged. It is noteworthy that even for a relatively large ratio of 32 between $\min(L_x, L_z)/\lambda$, the asymptotic DoF $\lfloor \frac{\pi L_x L_z}{\lambda^2} \rfloor$ still does not serve as the upper bound of the EDoF in various settings as shown in Fig. 10, indicating that the actual rank of the composite channel $\tilde{\mathbf{B}}$ in (18) is larger than $\lfloor \frac{\pi L_x L_z}{\lambda^2} \rfloor$ in this case, since EDoF should lie between 0 and the channel rank [12].

V. CONCLUSION

In this paper, we have systematically investigated the characteristics of eigenvalues of the spatial correlation matrix at the RIS and those of the composite channel matrix with RISs at both the transmitter and receiver. More importantly, we have also studied the EDoF of the

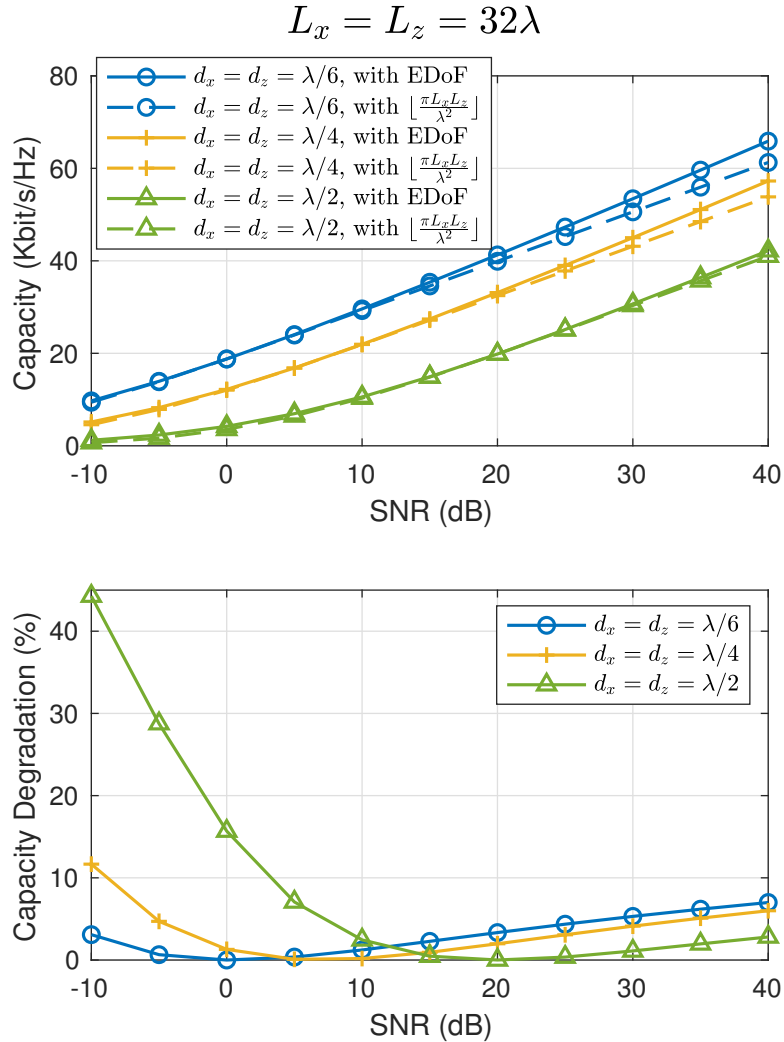


Fig. 11: Upper: Capacity versus receive SNR for both EDoF and the DoF $\lfloor \frac{\pi L_x L_z}{\lambda^2} \rfloor$ for various element spacing d_x and d_z with $L_x = L_z = 32\lambda$. Lower: Capacity degradation of using the DoF $\lfloor \frac{\pi L_x L_z}{\lambda^2} \rfloor$ against the EDoF for various element spacing d_x and d_z with $L_x = L_z = 32\lambda$.

composite channel that yields the maximum capacity. Distinct from the DoF of RISs in the existing literature which ignores the SNR condition, EDoF is affected by SNR as well as the spatial correlation. Although the analysis in this paper is conducted for the isotropic scattering environment, it is expected that similar trends on the EDoF will occur for non-isotropic scattering, with fewer EDoF in general due to more severe spatial correlation [29].

REFERENCES

- [1] T. L. Marzetta, "Noncooperative cellular wireless with unlimited numbers of base station antennas," *IEEE Transactions on Wireless Communications*, vol. 9, no. 11, pp. 3590–3600, Nov. 2010.
- [2] H. Yan and I.-T. Lu, "Asynchronous reception effects on distributed massive MIMO-OFDM system," *IEEE Transactions on Communications*, vol. 67, no. 7, pp. 4782–4794, Jul. 2019.
- [3] —, "BS-UE association and power allocation in heterogeneous massive MIMO systems," *IEEE Access*, Oct. 2020.
- [4] H. Yan and H. Yang, "Pilot length and channel estimation for massive MIMO IoT systems," *IEEE Transactions on Vehicular Technology*, vol. 69, no. 12, pp. 15 532–15 544, Dec. 2020.
- [5] H. Yan, A. Ashikhmin, and H. Yang, "A scalable and energy-efficient IoT system supported by cell-free massive MIMO," *IEEE Internet of Things Journal*, vol. 8, no. 19, pp. 14 705–14 718, Oct. 2021.
- [6] A. Pizzo, T. L. Marzetta, and L. Sanguinetti, "Spatially-stationary model for Holographic MIMO small-scale fading," *IEEE Journal on Selected Areas in Communications*, vol. 38, no. 9, pp. 1964–1979, Sep. 2020.
- [7] C. Huang, S. Hu, G. C. Alexandropoulos, A. Zappone, C. Yuen, R. Zhang, M. D. Renzo, and M. Debbah, "Holographic MIMO surfaces for 6G wireless networks: Opportunities, challenges, and trends," *IEEE Wireless Communications*, vol. 27, no. 5, pp. 118–125, Oct. 2020.
- [8] C. L. Holloway, E. F. Kuester, J. A. Gordon, J. O'Hara, J. Booth, and D. R. Smith, "An overview of the theory and applications of metasurfaces: The two-dimensional equivalents of metamaterials," *IEEE Antennas and Propagation Magazine*, vol. 54, no. 2, pp. 10–35, Apr. 2012.
- [9] S. Sun, Z. Ye, L. Guo, and N. Sun, "Wide-incident-angle chromatic polarized transmission on trilayer silver/dielectric nanowire gratings," *Journal of the Optical Society of America B*, vol. 31, no. 5, pp. 1211–1216, May 2014.
- [10] E. Bjornson and L. Sanguinetti, "Rayleigh fading modeling and channel hardening for reconfigurable intelligent surfaces," *IEEE Wireless Communications Letters*, vol. 10, no. 4, pp. 830–834, Apr. 2021.
- [11] S. Sun and H. Yan, "Small-scale spatial-temporal correlation and degrees of freedom for reconfigurable intelligent surfaces," *IEEE Wireless Communications Letters*, pp. 1–1, 2021.
- [12] D.-S. Shiu, G. Foschini, M. Gans, and J. Kahn, "Fading correlation and its effect on the capacity of multielement antenna systems," *IEEE Transactions on Communications*, vol. 48, no. 3, pp. 502–513, Mar. 2000.
- [13] C.-N. Chuah, D. Tse, J. Kahn, and R. Valenzuela, "Capacity scaling in MIMO wireless systems under correlated fading," *IEEE Transactions on Information Theory*, vol. 48, no. 3, pp. 637–650, Mar. 2002.
- [14] N. Chiurtu, B. Rimoldi, and E. Telatar, "Dense multiple antenna systems," in *Proceedings 2001 IEEE Information Theory Workshop (Cat. No.01EX494)*, 2001, pp. 108–109.
- [15] S. Sun and H. Yan, "Channel estimation for reconfigurable intelligent surface-assisted wireless communications considering Doppler effect," *IEEE Wireless Communications Letters*, vol. 10, no. 4, pp. 790–794, Apr. 2021.
- [16] A. Moustakas, H. Baranger, L. Balents, A. Sengupta, and S. Simon., "Communication through a diffusive medium: Coherence and capacity," *Science*, vol. 287, pp. 287–290, Jan. 2000.
- [17] A. Tulino, A. Lozano, and S. Verdu, "Impact of antenna correlation on the capacity of multiantenna channels," *IEEE Transactions on Information Theory*, vol. 51, no. 7, pp. 2491–2509, Jul. 2005.
- [18] S. Wei, D. Goeckel, and R. Janaswamy, "On the asymptotic capacity of MIMO systems with antenna arrays of fixed length," *IEEE Transactions on Wireless Communications*, vol. 4, no. 4, pp. 1608–1621, Jul. 2005.
- [19] E. Telatar, "Capacity of multi-antenna Gaussian channels," *European Transactions on Telecommunications*, vol. 10, no. 6, pp. 585–595, Nov.-Dec. 1999.
- [20] F. Riesz and B. Nagy, *Functional Analysis*. New York: Frederick Unger, 1955.

- [21] A. Pizzo, T. L. Marzetta, and L. Sanguinetti, "Degrees of freedom of Holographic MIMO channels," in *2020 IEEE 21st International Workshop on Signal Processing Advances in Wireless Communications (SPAWC)*, 2020, pp. 1–5.
- [22] S. H. Simon and A. L. Moustakas, "Eigenvalue density of correlated complex random wishart matrices," *Physical Review E*, vol. 69, pp. 065 101–1–065 101–4, Jun. 2004.
- [23] Z. D. Bai and J. W. Silverstein, "Exact separation of eigenvalues of large dimensional sample covariance matrices," *The Annals of Probability*, vol. 27, no. 3, pp. 1536–1555, 1999.
- [24] S. Sun, T. S. Rappaport, M. Shafi, and H. Tataria, "Analytical framework of hybrid beamforming in multi-cell millimeter-wave systems," *IEEE Transactions on Wireless Communications*, vol. 17, no. 11, pp. 7528–7543, Nov. 2018.
- [25] Y. Q. Yin, Z. D. Bai, and P. R. Krishnaiah, "On the limit of the largest eigenvalue of the large dimensional sample covariance matrix," *Probability Theory and Related Fields*, no. 78, pp. 509–521, 1988.
- [26] B.-Y. Xi and F. Zhang, "Inequalities for selected eigenvalues of the product of matrices," in *Proceedings of the American Mathematical Society*, vol. 147, no. 9, 2019, pp. 3705–3713.
- [27] F. S. Woods, *Advanced Calculus*. Boston, MA, USA: Ginn, 1926.
- [28] S. Sun, S. Moon, and J.-K. Fwu, "Practical link adaptation algorithm with power density offsets for 5G uplink channels," *IEEE Wireless Communications Letters*, vol. 9, no. 6, pp. 851–855, Jun. 2020.
- [29] S. Sun and H. Yan, "Small-scale spatial-temporal correlation modeling for reconfigurable intelligent surfaces." [Online]. Available: <https://arxiv.org/pdf/2105.15096v1.pdf>.